



Ultralong porous ZnO nanobelt arrays grown directly on fluorine-doped SnO₂ substrate for dye-sensitized solar cells

Xiaoyan Hu^a, Bojun Heng^a, Xinqi Chen^a, Bixiao Wang^a, Daming Sun^a, Yongming Sun^b, Wei Zhou^b, Yiwen Tang^{a,*}

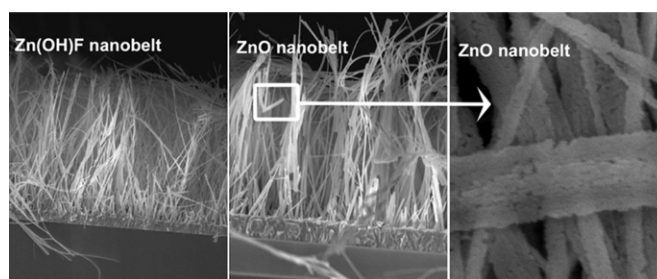
^a Institute of Nano-science and Technology, Central China Normal University, Wuhan 430079, China

^b Wuhan Jiawei Photovoltaic Lighting Co., Ltd, China

HIGHLIGHTS

- Arrays of novel ultralong nanoporous ZnO nanobelts (NBs) have been successfully obtained.
- This is the first report on the DSSCs that employ ultralong porous ZnO NB arrays as the photoanode.
- A high conversion efficiency (η) of 3.28% for a 27 μm thick film was obtained at 0.9 suns.

GRAPHICAL ABSTRACT



ARTICLE INFO

Article history:

Received 6 April 2012

Received in revised form

30 May 2012

Accepted 1 June 2012

Available online 12 June 2012

Keywords:

Ultralong nanoporous

High internal surface area

Dye-sensitized solar cell

ABSTRACT

Arrays of novel ultralong nanoporous ZnO nanobelts (NBs) are developed with a two-step synthesis strategy. This strategy combines two processes, a rapid hydrothermal synthesis of vertically aligned ultralong Zn(OH)F NB arrays directly on fluorine-doped tin oxide (FTO) at pH = 8.5 and conversion of a pyrolysis Zn(OH)F NB intermediate into nanoporous ZnO NB. Two factors play crucial roles in the rapid synthesis of ultralong Zn(OH)F nanobelt (NB) arrays, i.e., the pretreatment of the FTO substrate before entering the aqueous solution of Zn²⁺ (2 M) and the presence of excess F[−] in the hydrothermal reaction solution. Upon the subsequent pyrolysis of the Zn(OH)F precursor at 500 °C for 2 h, ultralong nanoporous ZnO NB arrays are successfully generated. In addition, every NB is composed of a large number of nanocrystals and nanopores, which exhibit preferred orientation. Dye-sensitized solar cells (DSSCs) based on the ultralong porous ZnO NB arrays are assembled, and a high conversion efficiency (η) of 3.28% for a 27 μm thick film is obtained at 0.9 suns. This can be attributed to the high internal surface area and pronounced light scattering, as well as a good electron collection efficiency comparable with that of ZnO nanorod (NR)-based DSSCs.

© 2012 Elsevier B.V. All rights reserved.

1. Introduction

Dye-sensitized solar cells (DSSCs) based on the photosensitization of an oxide semiconductor by adsorbed organic dyes or metalloorganic complex dyes have recently emerged as the most

promising candidate systems [1–4]. Compared with commonly used TiO₂ photoanodes, ZnO photoanodes have been intensively investigated due to their similar band gap, easier synthesis and higher electron mobility [5–9]. Moreover, ZnO can be easily processed into various nanostructures, such as nanoparticles, nanowires, nanotubes, and tetrapods, providing numerous options for optimizing the electrode morphology so as to improve the charge collection [10–13]. Among various morphologies of the electrode

* Corresponding author. Tel.: +86 27 67867947; fax: +86 27 67861185.

E-mail address: ywtang@phy.ccnu.edu.cn (Y. Tang).

for ZnO-based DSSCs, one-dimensional (1D) ZnO nanostructures directly grown on F-doped SnO₂ glass (FTO) substrates have been identified as a promising class of candidate to improve the performance of DSSCs since they offer direct electrical pathways for photogenerated electrons and could increase the electron transport rate [14]. However, one key challenge of using 1D nanostructures in DSSCs is that, the 1D nanostructures have a low internal surface area for dye loading and inefficient light-scattering centers compared with those of mesoporous films [15–18]. Thus the conversion efficiency (η) values are much lower than those of mesoporous films (e.g. only 1.5% for ZnO nanowires [19]).

In this regard, Ku et al. presented an approach to enlarge the internal surface area within the photoanode by introducing ZnO nanoparticles onto the original 1D ZnO nanowires and obtained an efficiency of 3.2% [20]. Gao also fabricated DSSCs by using multi-layer assemblies of ZnO nanowire arrays and the efficiency has been greatly enhanced [21]. Although some progress has been made, both of the two fabrications processes are multiple and complex in character. Moreover, during the synthesis of multilayer assemblies of ZnO nanowire arrays, the fusion of wires at the root is large due to the widening of the wires as they lengthen. Therefore, building aligned 1D nanostructure arrays with large internal surface area by using low-cost methods remains challenging.

In our previous work, we have developed a novel two-step strategy to fabricate porous ZnO prism arrays composed of nanograins with high orientation order and nanopores [22]. The two-step synthesis approach comprised a wet chemical process at pH = 6.0 to grow Zn(OH)F prism arrays and a pyrolysis of Zn(OH)F intermediates into F-doped ZnO without altering the prism morphology. However, such a prism array has a limited roughness factor (RF), defined as the ratio of the actual surface area to the projected area of the structure, due to the short length (5 μ m). After understanding the formation mechanism of Zn(OH)F prisms, we have explored other experimental parameters such as pH value, reaction temperature, and the amount of NH₄F contained. It was found that a porous nanobelt (NB) array with an increased RF was obtained under optimal conditions. In the present work we present a simple hydrothermal route towards a rapid synthesis of ultralong Zn(OH)F NB arrays directly on FTO at pH = 8.5, which were then used as the precursor to prepare the porous ZnO nanostructures with the same shape by pyrolysis. Here, a key strategy for rapid synthesis of aligned Zn(OH)F NB directly on FTO is using the adsorption of Zn²⁺ on FTO as nuclei of Zn(OH)F formation and the excess F[−] as a morphology controlling agent acting on the Zn(OH)F. By using this method, the novel hierarchically porous NB array film not only maintains the characteristics of a vertically aligned nanowire for affording fast electron transport channels, but also increases the internal surface area for dye adsorption and light harvesting. DSSCs based on the ultralong nanoporous ZnO NB arrays were assembled, and a high efficiency of 3.28% was obtained, owing to high dye loading and good light harvesting.

2. Experimental

2.1. Preparation of ultralong nanoporous ZnO NB films

Our specific experimental procedure for the rapid growth of ultralong Zn(OH)F NB arrays was as follows. The F-doped SnO₂ glass substrates (FTO, 10–15 Ω sq^{−1}, Japan, Asahi Company) were first cleaned thoroughly by consecutive sonication in acetone, ethanol and isopropanol. The FTO substrates were then immersed in an aqueous solution of Zn²⁺ (2 M) (taking Zn(NO₃)₂ as an example) at room temperature for 3 h. After being dried, the treated FTO was ready for subsequent Zn(OH)F NB array growth. Then 80 mL aqueous growth solution consisting of 0.03 M

Zn(NO₃)₂·6H₂O, 0.3 M NH₄F, and 0.25 M NH₃·H₂O was transferred into Teflon-lined stainless steel autoclaves. At this moment the pH of aqueous growth solution was 8.5. A piece of treated FTO substrate was immersed into the reaction solution and the autoclave sealed and maintained at 120 °C for 3 h and then gradually cooled to room temperature. The as-obtained Zn(OH)F arrays were rinsed with distilled water and calcined in air at 500 °C for 2 h to transform them to ZnO.

2.2. Characterization

The products were characterized by a Bruker D8 Advance X-ray diffractometer (XRD) with monochromatized CuK α radiation (λ = 1.5418 Å) recorded with 2 θ ranging from 10° to 80°. The morphologies of the samples were observed with scanning electron microscopy (SEM, JSM-6700F; 5 kV). The structural properties were analyzed by transmission electron microscopy (TEM) and high resolution transmission electron microscopy (HRTEM) using a JEM-2010FEF instrument; 200 kV. The UV–vis absorption spectra were obtained on a Perkin Elmer Lambda35 spectrometer. The X-ray photoelectron spectrum (XPS) was recorded on a VG Multilab 2000X spectrometer using Al K-X-ray as the excitation source.

2.3. DSSC fabrication and performance measurements

The porous ZnO NB electrodes on FTO were immersed in a 0.5 mM ethanol solution containing the ruthenium complex *cis*-bis(2,2′-bipyridyl-4,4′-dicarboxylato)-ruthenium(II)-bis-tetrabutylammonium (commercially known as N719 dye) (Solaronix, Aubonne, Switzerland) for 3 h at room temperature. The sensitized ZnO electrode was assembled with a platinum-coated FTO counter electrode, and the gap between the two electrodes was controlled by using a 25 μ m thick Surlyn film (China). The electrolyte solution comprising 0.5 M I₂, 0.05 M LiI, 0.5 M 4-*tert*-butylpyridine, 0.6 M methylhexylimidazolium iodide in acetonitrile filled the gap by capillary action. The active cell area was typically \sim 8 mm². The photoelectrochemical tests of the DSSCs were performed under one sun condition using a solar light simulator (Oriel, 69911, AM 1.5 globe) with 90 mW cm^{−2} light output. The photocurrent-voltage (*I*–*V*) characteristics were obtained using a Princeton Applied Research Model 263A Potentiostat/Galvanostat. Incident photon-current conversion efficiency (IPCE) was recorded on a DC Power Meter (Model 2931-C, Newport Co.) under irradiation of a 300 W xenon lamp light source with a motorized monochromator (Oriel). The xenon lamp was powered by an Arc Lamp Power Supply (Model 69920, Newport Co.). The amount of dye loading was determined by desorbing the dye within the photoanode with 0.2 mM NaOH solution and measuring the optical absorbance with a UV–vis spectrophotometer. The intensity-modulated photocurrent spectroscopy (IMPS) test was performed using a green light emitting diode (λ_{max} = 535 nm) driven by a Zahner Zenium. The LED provided both the direct current (dc) and alternating current (ac) components of the illumination.

3. Results and discussion

3.1. Structure and morphology of ultralong Zn(OH)F NB arrays

Fig. 1 shows the XRD pattern of the intermediate product prepared by immersion in the Zn(NO₃)₂ solution followed by a hydrothermal reaction (120 °C for 3 h). All the peaks are indexed to be orthorhombic Zn(OH)F (JCPDS file No. 74–1816). No impurity peaks were detected, indicating the high purity of the as-prepared Zn(OH)F.

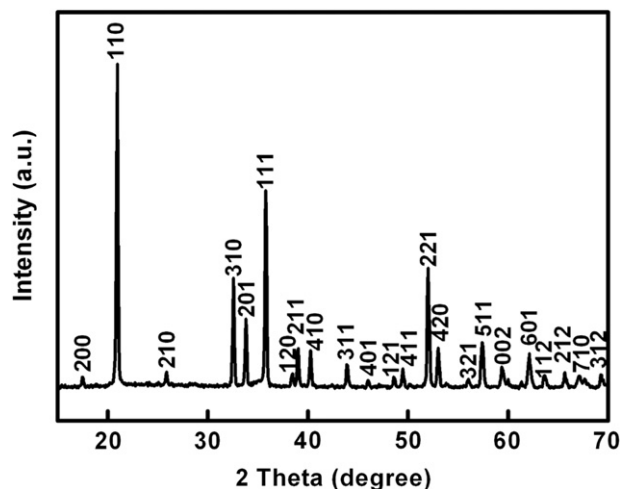


Fig. 1. XRD pattern of Zn(OH)F prepared by immersion in Zn(NO₃)₂ solution followed by a single hydrothermal reaction (120 °C for 3 h).

A typical top-view SEM image (Fig. 2a) over a large area has been made, which reveals the large-scale growth of ultralong Zn(OH)F NB arrays directly on the FTO substrate. From the top-view of the NBs, we can clearly see that the tip of NBs cross each other with polydispersed widths in the range of 60–300 nm. Fig. 2b–d display

the tilted-view SEM images of the Zn(OH)F NB arrays, after 1, 2, and 3 h hydrothermal growth, respectively. The Zn(OH)F NBs are aligned in a dense array that is perpendicular to the substrate surface. The elongation becomes larger with increasing growth time progressing from 7 μm to 19 μm then to 32 μm. By such a hydrothermal process carried out for 3 h, vertically aligned Zn(OH)F NBs up to 32 μm long can be obtained without fusing the roots of the NBs and increasing the width of the NBs. This result clearly demonstrated that as the NBs grew vertically, the growth of side walls was effectively suppressed.

Fig. 3a shows a TEM image of a single NB with width of ~200 nm. The nanobelt is transparent to the electron beam, since the copper grid pattern below the belt can be clearly seen, indicating that the belt is very thin. The corresponding selected area electron diffraction (SAED) shown in Fig. 3b and captured from the circled part, indicates that the NBs are single crystalline structures and the SAED pattern can be indexed into diffraction spots of the [010] zone. The NBs grow along the [100] direction and the flat surface is identified as a (010) facet.

3.2. Formation mechanism of the ultralong Zn(OH)F NB and ultralong nanoporous ZnO NB arrays

In order to probe formation mechanism of the Zn(OH)F NB arrays directly grown on FTO substrates, we carried out a systematic investigation. We note that the immersion in the Zn(NO₃)₂

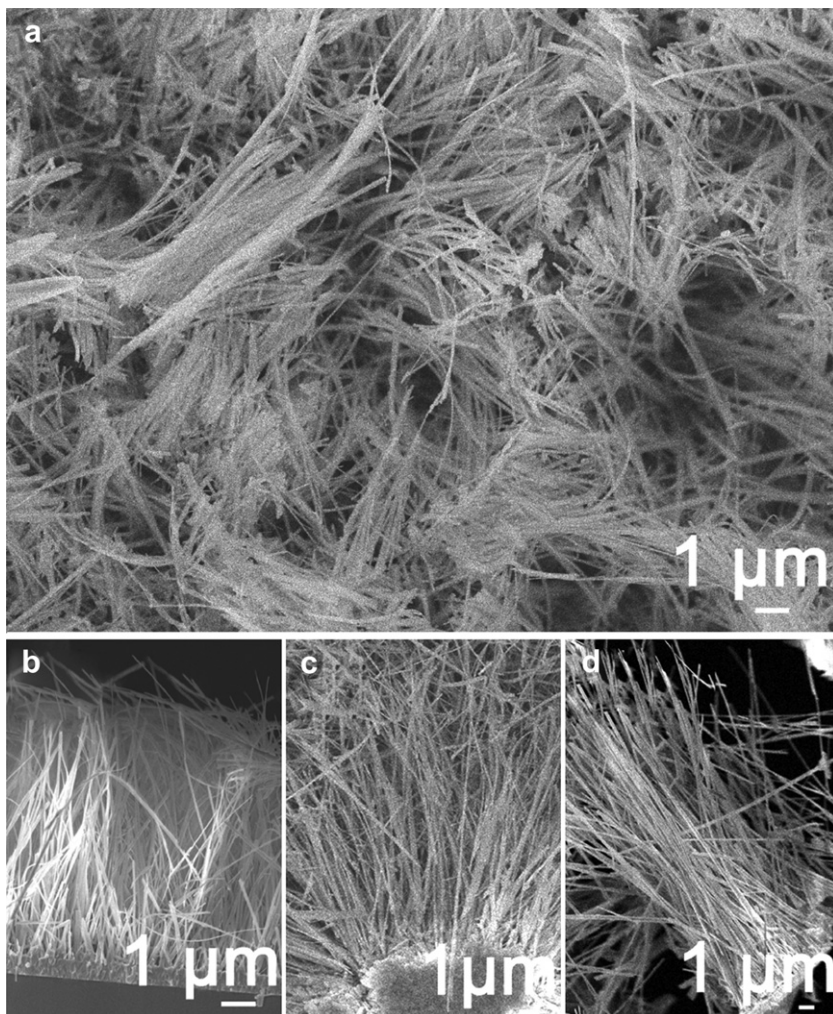


Fig. 2. (a) The top-view SEM image of the Zn(OH)F NB array. (b–d) The tilted-view SEM images of the Zn(OH)F NB arrays after 1, 2, and 3 h hydrothermal growth, respectively.

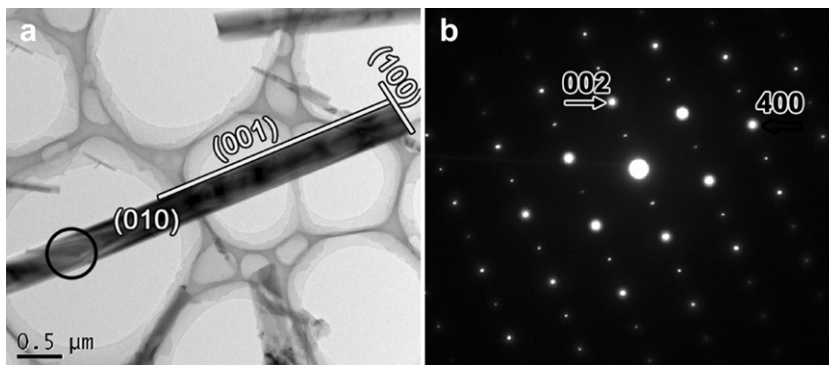


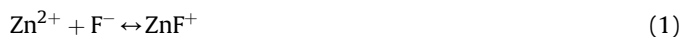
Fig. 3. (a) TEM image and (b) SAED pattern of the Zn(OH)F NB.

solution before the hydrothermal process is crucial in order to adsorb a large amount of Zn^{2+} on the active sites of the entire FTO sample. Without the treatment in 2 M $\text{Zn}(\text{NO}_3)_2$ solution the NBs randomly distribute on the FTO substrate and are intercrossed, as shown in Fig. S1a in the supporting information. Thus, preceding the hydrothermal process and after treatment in an aqueous solution of 2 M $\text{Zn}(\text{NO}_3)_2$, Zn^{2+} ions interact with the conducting layer on the FTO and adsorb on its surface. Once the hydrothermal reaction starts, the OH^- and F^- ions are prone to react with the Zn^{2+} adsorbed on the FTO surface rather than in the solution and subsequently produce nuclei of Zn(OH)F. The nucleation and growth of the NBs is followed by the reaction of F^- , OH^- , and Zn^{2+} diffusing from the solution. As a further confirmation of the role of Zn^{2+} adsorbed on FTO substrate, other salts, i.e., ZnCl_2 , $\text{Zn}(\text{OAc})_2$ have been used to replace $\text{Zn}(\text{NO}_3)_2$, similar morphologies of Zn(OH)F can be obtained (see Fig. S1b and c in the supporting information). The corresponding tilted views (in Fig. S2a and b) of the samples with the FTO substrates pretreatment with the ZnCl_2 and $\text{Zn}(\text{OAc})_2$ solution respectively indicate the role of Zn^{2+} .

It was found that the presence of excess F^- in the hydrothermal reaction solution played a dual major role in the fast growth of highly oriented NB arrays. To decipher the function of F^- , we performed a series of syntheses by altering the concentration of NH_4F in the raw material solution, and the results are summarized in Fig. S3. At a low concentration of F^- (0.15 M), there were no ultralong NBs present but only nanorods (NRs) with lengths of 2 μm randomly distributed on the whole substrate without any preferred orientation (Fig. S3a). Further increasing the addition of NH_4F to 0.24 M resulted in a mixture of NBs and NRs, as shown in Fig. S3b. When the concentration of NH_4F reached 0.3 M, a whole NB morphology with widths ranging from 60 to 300 nm resulted (Fig. S3c). The corresponding XRD patterns for the above three samples were shown in patterns a–c of Fig. S3d, respectively. It is notable that at the concentration of 0.15 M, ZnO rather than Zn(OH)F, precipitates and this is reasonable because a large amount of OH^- contained in the reaction solution reacts with Zn^{2+} . With the NH_4F concentration increasing to 0.24 M, the intensity of the diffraction peaks from ZnO (JCPDS file No. 80-0075) marked with * in pattern b of Fig. S3d decreased. At the same time, Zn(OH)F started to precipitate, which is confirmed by the diffraction peaks from Zn(OH)F (JCPDS file No. 74-1816) marked by ● in pattern b of Fig. S3d. At 0.3 M NH_4F , the prevalent diffraction peaks could be indexed to Zn(OH)F (JCPDS file No. 74-1816) in patterns c of Fig. S3d. From the above experimental results, it is clearly seen that at the low content of NH_4F , the precipitation of ZnO has occurred. At higher NH_4F content, Zn(OH)F precipitates. According to the usual theory of crystal growth [23], homogenous nucleation for film formation nucleation occurs at higher supersaturation levels. Thus

in the Zn(OH)F deposition process, NH_4F acts as an agent to control the supersaturation of Zn(OH)F through the formation of ZnF^+ which results in nucleation and growth of Zn(OH)F. In addition, according to the report of Satio on the pH dependence of the concentration of the zinc species for investigating the deposition manner of Zn(OH)F [24], ZnF^+ concentration decreases and the concentrations of ammine complexes increase with increasing pH. Thus in our present work of Zn(OH)F NB arrays growing at pH 8.5, there is excessive F^- left in the growth solution. Similar to the analysis by Yang [25], the excessive F^- in the hydrothermal reaction solution is believed to exert a dual role. The one role involves adsorption. Due to the anisotropy in adsorption stability of the F^- , F^- is adsorbed onto a certain crystallographic plane more strongly than the others, which lowers the surface energy of the bound plane and hinders the growth of the crystal in some directions. Therefore, in our system, it might be used as the crystallographic controlling agent of Zn(OH)F, owing to the attractive interaction of Zn–F. Once Zn(OH)F nuclei form, F^- would be preferentially adsorbed on the (010) plane of the nucleus and thus retard the growth of Zn(OH)F along the [010] direction and, at the same time, stimulate the growth along the [100] direction. The second role occurs with the introduction of F^- , which results in the rate of the nucleation of Zn(OH)F on the FTO substrate being much faster than that of the diffusion of Zn^{2+} from the substrate to the reaction solution, and this results in formation of a highly oriented NB array. Because of the high growth rate, our method is particularly useful for growing ultralong Zn(OH)F NB arrays.

Based on the above discussions, the F^- mediated formation process in the hydrothermal synthesis of the unique ultralong Zn(OH)F NB arrays is schematically illustrated in Fig. 4a–c. The corresponding formation process is assumed to involve three ionic reactions (1–2).



Zn(OH)F was reported to be a precursor of ZnO. [26]. Upon the subsequent pyrolysis of the Zn(OH)F at 500 °C for 2 h, Zn(OH)F was transformed into nanoporous ZnO (Fig. 4d).

3.3. Structure and morphology of the ultralong nanoporous ZnO NBs

The transformed product was confirmed by XRD pattern (in Fig. 5a). The XRD pattern was indexed into a hexagonal phase of ZnO (JCPDS file No. 80-0075), suggesting that the precursor Zn(OH)F has been completely transformed into ZnO. The typical XPS spectrum of the hexagonal phase of ZnO which was obtained

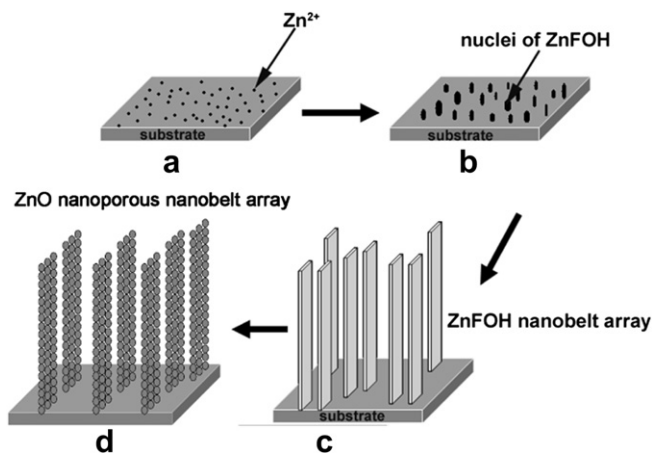


Fig. 4. Schematic illustration of the formation process of the ultralong nanoporous ZnO NB array.

through subsequent pyrolysis of the precursor Zn(OH)F at 500 °C for 2 h is shown in Fig. 5b. The binding energies in the XPS spectrum were calibrated using that of C1s (284.6 eV). The binding energies of Zn 2p_{3/2} and Zn 2p_{1/2} were identified at 1023.35 eV and

1045.1 eV, respectively. The binding energy of O1s was found at 532.1 eV, which is very close to the reported values in the literature. There is no peak of F1s located at 532.1 eV present in the spectrum, suggesting that no F was left into the ZnO crystal lattice after annealing at 500 °C for 2 h.

Fig. 6a–c display the cross sectional images of ZnO arrays obtained by the pyrolysis of the intermediate Zn(OH)F through 1 h, 2 h, and 3 h hydrothermal reaction respectively. It can be seen that ZnO arrays have similar shapes and size distributions as those of the intermediate Zn(OH)F arrays. The only subtle difference is that the length of ZnO has become slightly smaller than that of the Zn(OH)F intermediate owing to the high temperature calcination effect. However, unlike the intermediate Zn(OH)F NB, every ZnO NB is composed of numerous nanocrystals with surrounding mesopores, as shown in Fig. 6d. From the high-magnification SEM image (Fig. 6e) it can be distinctly seen that the nanocrystals and nanopores are in the range of 5–20 nm and every nanocrystal is well attached to the neighboring nanocrystal. The belt structure is maintained because there are nanocontacts between each of the nanoparticles, which prevent structural collapse during the release of HF. Overall top-view SEM observations (Fig. 6f) show that there are polydispersed channels along the NBs which are beneficial for effective light scattering.

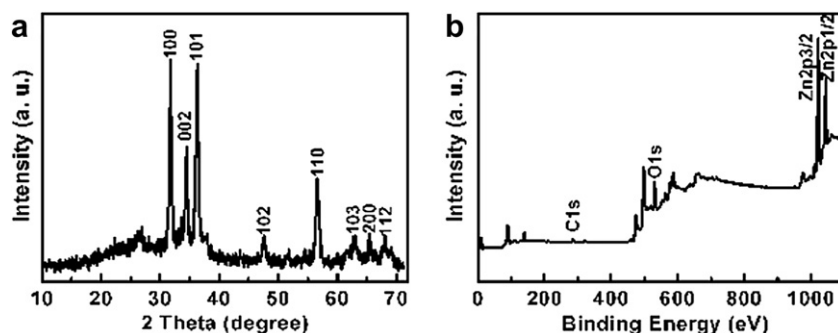


Fig. 5. (a) XRD pattern and (b) XPS spectrum of the obtained ZnO NB array.

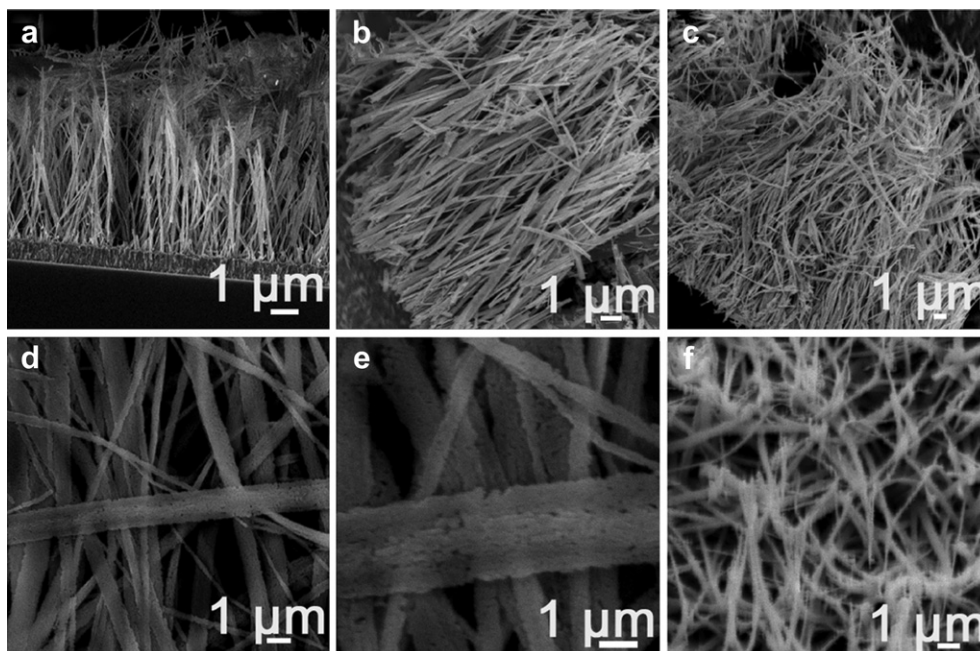


Fig. 6. (a–c) The cross sectional SEM images of ZnO arrays obtained by pyrolysis of the intermediate Zn(OH)F through 1 h, 2 h, and 3 h hydrothermal reaction respectively. (d) Low- and (e) high-magnification SEM images of ZnO NBs. (f) The top-view SEM image of the ZnO NBs.

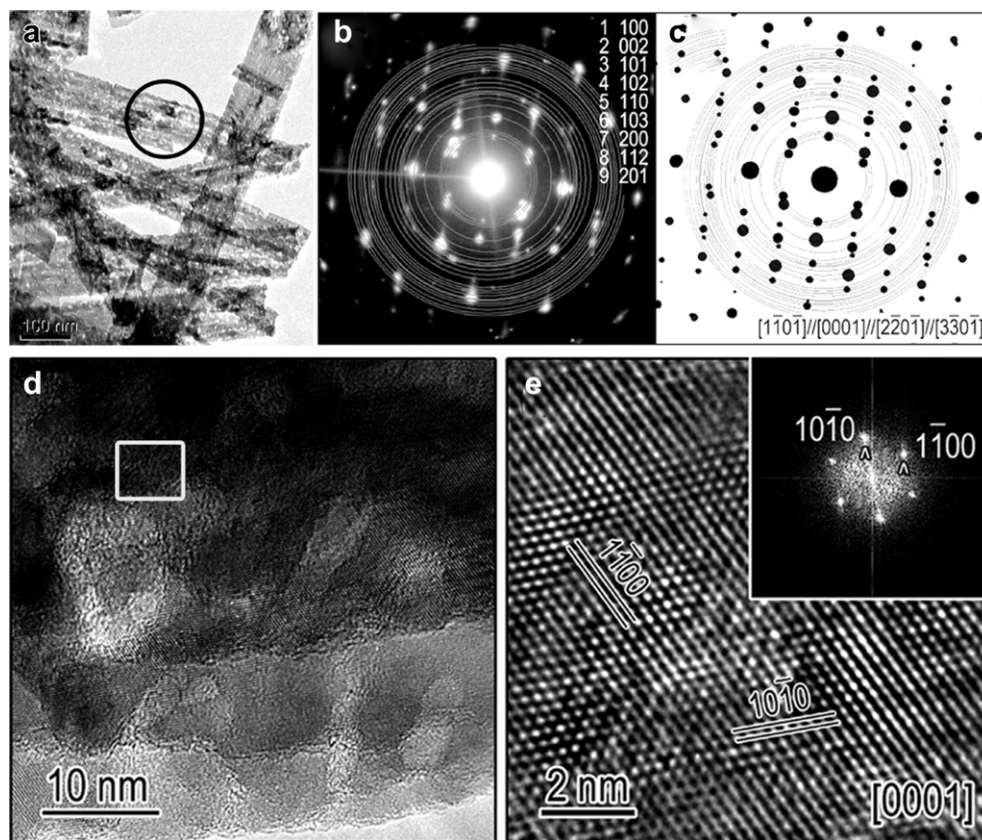


Fig. 7. (a) TEM image and (b) corresponding SAED pattern of the nanoporous ZnO NB. (c) Simulated SAED pattern of the nanoporous ZnO NBs. (d) HRTEM image and (e) enlarged HRTEM taken from the square in panel (d) with its corresponding FFT pattern inset.

The resulting nanoporous ZnO NBs were subjected to further investigations by TEM, SAED, and HRTEM. The TEM image (Fig. 7a) confirms that the belt structure comprises a large number of individual nanocrystals with surrounding pores. The isolated symmetrical bright diffraction spots in the SAED pattern in Fig. 7b which is recorded from the circled part in TEM image indicate that most of the nanocrystals have oriented attachment. The formation of these porous ZnO NBs might be due to the release of HF from the original Zn(OH)F NBs during pyrolysis. The simulated SAED pattern with the approximate crystallographic relationship of the hexagonal ZnO (Fig. 7c) agrees well with the experimental one. The typical HRTEM image of an individual ZnO NB shown in Fig. 7d exhibits clear and coherent lattice fringes running through the whole porous belt. Further, it is obvious that several nanocrystals are oriented and attached to neighboring crystals with nanopores in the range of 5–20 nm. The enlarged image of the framed area, and the corresponding Fourier Transform (FFT) pattern inset are shown in Fig. 7e. The measured lattice spacing from HRTEM corresponds well to the and crystal planes of hexagonal ZnO. Above all, the results of both SAED and HRTEM indicate that the ZnO NBs are composed of well attached crystals with oriented attachments.

3.4. Photovoltaic properties of the ultralong nanoporous ZnO based DSSCs

The novel hierarchical structure of the ZnO NBs provides an ideal electrode structure for DSSCs. Table 1 and Fig. 8a illustrate the current (J)–voltage (V) characteristics and photovoltaic parameters of the DSSCs prepared using ZnO NB arrays through the hydrothermal reaction times of 1 h (5 μm), 2 h (12 μm), and 3 h (27 μm), respectively. As expected, increasing the length of the NBs leads to

a significant increase in J_{sc} . When the NB length increases from 5 μm to 27 μm , J_{sc} increases from about 5.9 mA cm^{-2} to 10.2 mA cm^{-2} and the η increases from 1.36% to 3.28%. Apparently, the J_{sc} and η increase as the length of the ZnO NBs increases owing to the increase in the effective surface area. The 3.28% efficiency obtained from DSSCs based on 27 μm ZnO NB films is much higher than the reported value of 1.8% for the DSSCs based on ZnO NR films with the same length [27], indicating a significant improvement in the electron-collecting efficiency of photogenerated electrons in the ZnO NB-based photoanodes. Fig. 8b shows the IPCE measurements for the DSSCs fabricated using ZnO NB arrays with the three different lengths. As can be seen, increasing the total length of the NBs improves IPCE over the entire wavelength region of 380–720 nm. This is in good agreement with the stepwise increasing of J_{sc} . Another important feature observed in these IPCE curves is a red-shift of the peak as the length of the NB increases, which indicates that the spectral absorption range can be effectively broadened and strengthened by increasing the length of the sensitized ZnO NBs. The maximum IPCE value is up to 50% for 27 μm length ZnO NB films.

Such a high density, ultralong nanoporous NB structure makes the ZnO NB photoanode possess advantages in the following

Table 1

Photovoltaic parameters of the DSSC using ZnO NB arrays prepared through hydrothermal reaction time of 1 h (5 μm), 2 h (12 μm), and 3 h (27 μm) as photoanodes, respectively.

ZnO NB film	J_{sc} (mA cm^{-2})	V_{oc} (mV)	FF (%)	η (%)
5 μm	5.9	0.44	0.35	1.36
12 μm	7.5	0.41	0.47	2.09
27 μm	10.2	0.46	0.51	3.28

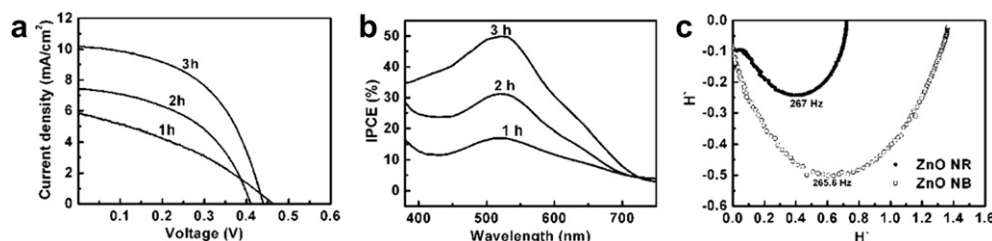


Fig. 8. (a) J - V curves and (b) IPCE curves of DSSCs using ZnO NB arrays prepared through a hydrothermal reaction time of 1 h (5 μm), 2 h (12 μm), and 3 h (27 μm), respectively as photoanodes. (c) Complex plots of ZnO NB-based and NR-based DSSCs, respectively, obtained from IMPS measurements.

aspects, which greatly benefit the performance of the ZnO NB-based DSSCs. First, compared with ZnO NR-based DSSCs, each ultralong nanoporous NB structure consists of nanoparticles and nanopores. This results in augmented internal surface area for dye-loading and a correspondingly large increase in J_{SC} . The measured surface area of ZnO NBs is 24.9 $\text{m}^2 \text{g}^{-1}$, much higher than that of ZnO NRs (2.78 $\text{m}^2 \text{g}^{-1}$). Moreover, the amount of dye adsorbed in the ZnO NB film and the ZnO NR film, both of which have the same length of 8 μm (both with 1 cm^2 area) were determined by measuring the elute dye concentrations with UV-vis absorption spectroscopy. It was found that the dye-loading of the NB-based photoanode was $2.07 \times 10^{-7} \text{ mol cm}^{-2}$, almost three times higher than that of the NR-based photoanode ($0.79 \times 10^{-7} \text{ mol cm}^{-2}$). The dye-loading results were consistent with their surface area data. Second, the novel ultralong nanoporous NBs not only maintain the fast electron transport channels of likewise aligned NR, but the nanoporous NBs are composed of densely packed grains with every grain oriented and attached to neighboring grains. Such a novel hierarchical structure would decrease the negative effects of electron grain boundary crossing in randomly dispersed nanoparticles, and is expected to enhance the electron transport in the ZnO NB film and reduce recombination. Finally, the micro-channels among the NBs and the pores in the NBs favor the penetration of the electrolyte into the matrix of the photoanode. Thus, the light-harvesting ability has been significantly improved.

To verify the analysis of the structural advantages of the ZnO NBs arrays, we have investigated the electron transport in the NB-based photoanode and ZnO NR-based photoanode using the IMPS (Fig. 8c). Here, ZnO NR arrays were prepared by hydrothermal synthesis [28], and both the photoanodes have the thickness of 8 μm . The intensity of the IMPS shows that the NB-based devices have a larger light response than that found for the NR-based devices. This notable increase in light response stems from sufficient dye-loading and the superior light-harvesting properties of ZnO NB-based DSSCs. The inverse of the frequency ($\tau_d = 1/2\pi f_{\text{min}}$) at the minimum of the IMPS arch represents the typical time interval from photoelectron injection to photoelectron arrival at the substrate. The calculated time interval τ_d is 0.599 ms and 0.596 ms in NB and NR films, respectively. In addition, from the equation $D_n = d^2/(2.35\tau_d)$, where d is the thickness of the photoelectrode (8 μm), the electron diffusion coefficients (D_n) in NB-based and NR-based systems are calculated to be $4.546 \times 10^{-4} \text{ cm}^2 \text{s}^{-1}$ and $4.569 \times 10^{-4} \text{ cm}^2 \text{s}^{-1}$, respectively. The slight difference in f_d and D_n indicates the photoelectron transport and collection process in ZnO NB-based photoanode is comparable with that in ZnO NR-based photoanode.

4. Conclusion

In summary, we developed a two-step synthesis strategy to synthesize novel ultralong nanoporous ZnO NB arrays, which combines a hydrothermal synthesis of vertically aligned ultralong

Zn(OH)F NB arrays directly on FTO and the pyrolysis of Zn(OH)F intermediate into ZnO with the same morphology. The key mechanism of rapid synthesis of ultralong Zn(OH)F NB arrays is that the pretreatment of FTO substrates into aqueous solution of Zn^{2+} (2 M) solution and the presence of excess F^- in the hydrothermal reaction solution. Upon the subsequent pyrolysis of the Zn(OH)F precursor at 500 $^\circ\text{C}$ for 2 h, ultralong nanoporous ZnO NB arrays were successfully obtained with every NB composed of a large amount of nanocrystals and nanopores processing preferential orientation. DSSCs based on the ultralong nanoporous ZnO NB arrays were assembled, and a high η of 3.28% for 27 μm thick nanoporous ZnO NB array based DSSCs was attained owing to high internal surface area, stronger light scattering, as well as good electron collection efficiency comparable to that of ZnO NR-based DSSCs. Such an approach to synthesize ultralong nanoporous ZnO NB arrays open a potential in other applications such as ultrasensitive chemical and biological sensors, light emitting diodes, nanogenerators, and so on.

Acknowledgment

Financially supported by the National Ministry of Science and Technology under grant No.2011YQ160002 and operation research funds for colleges from the China Ministry of Education (CCNU09A02011).

Appendix A. Supplementary material

Supplementary material associated with this article can be found, in the online version, at <http://dx.doi.org/10.1016/j.jpowsour.2012.06.004>.

References

- [1] M. Gratzel, *Inorg. Chem.* 44 (2005) 6841.
- [2] L. Alibabaei, M.K. Wang, R. Giovannetti, J. Teuscher, D. Di Censo, J.E. Moser, P. Comte, F. Pucciarelli, S.M. Zakeeruddin, M. Gratzel, *Energy Environ. Sci.* 3 (2010) 956.
- [3] T. Yoshida, K. Terada, D. Schlettwein, T. Oekermann, T. Sugiura, H. Minoura, *Adv. Mater.* 12 (2000) 1214.
- [4] A. Abboto, N. Manfredi, C. Marini, F. De Angelis, E. Mosconi, J.H. Yum, X.X. Zhang, M.K. Nazeeruddin, M. Gratzel, *Energy Environ. Sci.* 2 (2009) 1094.
- [5] M. Guo, P. Diao, S. Cai, *Chin. Chem. Lett.* 15 (2004) 1113.
- [6] M. Guo, P. Diao, X. Wang, S. Cai, *J. Solid State Chem.* 178 (2005) 3210.
- [7] Y. Gao, M. Nagai, T.C. Chang, J. Shyue, *J. Cryst. Growth Des.* 7 (2007) 2467.
- [8] K. Wang, J. Chen, W. Zhou, Y. Zhang, Y. Yan, J. Pern, A. Mascarenhas, *Adv. Mater.* 20 (2008) 3248.
- [9] J. Qian, P. Liu, Y. Xiao, Y. Jiang, Y. Cao, X. Ai, H. Yang, *Adv. Mater.* 21 (2009) 3663.
- [10] K. Keis, C. Bauer, G. Boschloo, A. Hagfeldt, K. Westermark, H. Rensmo, H. Siegbahn, *J. Photochem. Photobiol. A: Chem.* 148 (2002) 57.
- [11] C.Y. Jiang, X.W. Sun, G.Q. Lo, D.L. Kwong, J.X. Wang, *Appl. Phys. Lett.* 90 (2007) 263501.
- [12] K. Keis, L. Vayssieres, A. Hagfeldt, S.E. Lindquist, *Chem. Mater.* 13 (2001) 4395.
- [13] Y.F. Hsu, Y.Y. Xi, C.T. Yip, A.B. Djurisić, W.K. Chan, *J. Appl. Phys.* 103 (2008) 0803114.
- [14] W. Lee, M.C. Jeong, J.M. Myoung, *Acta Mater.* 52 (2004) 3949.
- [15] G. K. Mor, K. Shankar, M. Paulose, O.K. Varghese, C.A. Grimes, *Nano. Lett.* 6 (2006) 215.

- [16] X. Feng, K. Shankar, O.K. Varghese, M. Paulose, T.J. Latempa, C.A. Grimes, *Nano. Lett.* 8 (2008) 3781.
- [17] B. Liu, E.S. Aydil, *J. Am. Chem. Soc.* 131 (2009) 3985.
- [18] C. Xu, P. Shin, L. Cao, J. Wu, D. Gao, *Chem. Mater* 22 (2010) 143.
- [19] M. Law, L.E. Greene, J.C. Johnson, R. Saykally, P.D. Yang, *Nat. Mater.* 4 (2005) 455.
- [20] C.H. Ku, J.J. Wu, *Nanotechnology* 18 (2007) 505706.
- [21] C.K. Xu, J.M. Wu, U.V. Desai, D. Gao, *J. Am. Chem. Soc.* 133 (2011) 8122.
- [22] L.J. Luo, W. Tao, X.Y. Hu, T. Xiao, B.J. Heng, W. Huang, H. Wang, H.W. Han, Q.K. Jiang, J.B. Wang, Y.W. Tang, *J. Power Sources* 196 (2011) 10518.
- [23] K. Sawada, in: H. Ohtaki (Ed.), *Crystallization Process*, Wiley, Chichester, England, 1998.
- [24] N. Saito, H. Haneda, W. Seo, K. Koumoto, *Langmuir* 17 (2001) 1461.
- [25] H.G. Yang, C.H. Sun, S.Z. Qiao, J. Zou, G. Liu, S.C. Smith, H.M. Cheng, G.Q. Lu, *Nature* 453 (2008) 638.
- [26] F. Xu, L. Sun, M. Dai, Y. Lu, *J. Phys. Chem. C* 114 (2010) 15377.
- [27] C. Xu, P. Shin, L. Cao, D. Gao, *J. Phys. Chem. C* 114 (2010) 125.
- [28] Y.W. Tang, X.Y. Hu, M.J. Chen, L.J. Luo, B.H. Li, L.Z. Zhang, *Electrochim. Acta* 54 (2009) 2742.